# Influence of Te-Doping on Catalyst-Free VS InAs Nanowires

Nicholas A. Güsken[1,3], Torsten Rieger[1,3], Gregor Mussler[1,3], Mihail Ion Lepsa[2,3*] and Detlev Grützmacher[1,2,3]

## Abstract

We report on the growth of Te-doped catalyst-free InAs nanowires by molecular beam epitaxy on silicon (111) substrates. Changes in the wire morphology, i.e. a decrease in length and an increase in diameter have been observed with rising doping level. Crystal structure analysis based on transmission electron microscopy as well as X-ray diffraction reveals an enhancement of the zinc blende/(wurtzite+zinc blende) segment ratio if Te is provided during the growth process. Furthermore, electrical two-point measurements show that increased Te-doping causes a gain in conductivity. Two comparable growth series, differing only in As-partial pressure by about $1 \times 10^{-5}$ Torr while keeping all other parameters constant, were analyzed for different Te-doping levels. Their comparison suggests that the crystal structure is strongly affected and the conductivity gain is more distinct for wires grown at a comparably higher As-partial pressure.

**Keywords:** Nanowires, InAs, Te-doping, Transport, X-ray measurements, Polytypism

## Background

Nanowires (NWs) have attracted notable attention within the last decade as they are considered to constitute a promising building block for emerging and future technology. Their technical applications are diverse, ranging from field effect transistors and optical devices to solar cells [1, 2]. The broad applicability of NWs is based on their remarkable characteristics, such as a high aspect ratio, ultra-low power dissipation and, in case of InAs, the absence of a Schottky barrier at the interface with metal contacts [3–5]. The latter is due to the fact that InAs exhibits a surface accumulation layer, enabling ohmic contacting [6]. From the physics perspective, InAs NWs bear outstanding properties, i.e., a high electron mobility [7], a low effective mass [8], a large g-factor [9] and strong Rashba spin-orbit coupling [10, 11]. Due to this, they became an important ingredient regarding quantum information related research [5, 12–14].

InAs NWs are commonly grown via a vapor-liquid-solid (VLS) growth method using gold droplets as a catalyst. The use of Au presents at least two drawbacks. On the one hand, it incorporates as unintentional impurity in the

NWs degrading their material properties [2, 15, 16], on the other hand, the integration of already demonstrated important applications like NW field-effect transistors (FET) [17], tunnel FETs [18], photodetectors [19], etc., on the silicon-based technology is not possible. Thus, a catalyst-free growth in the vapor-solid (VS) mode developed previously was applied within this communication [20]. A part from the cubic zinc blende (ZB) phase, which is the stable phase in bulk III-V materials, the hexagonal wurtzite (WZ) phase is also present in nanowires. ZB-WZ polytypism and other defects like rotational twins and stacking faults are commonly reported. Phase pure, almost free of stacking faults InAs NWs can be obtained by Au-assisted VLS growth [21, 22] but not using the catalyst-free VS method [23–25]. These defects adversely impact the transport [26, 27] and optical properties [28].

One way to counteract the diminished charge transport is the use of doping, i.e., the incorporation of additional carriers. However, the well-established doping methods used for III-V compound semiconductor layers cannot simply be transferred to the wire structures. The nanowires have axial and radial growth facets with different crystal orientation and surface reconstructions resulting in highly anisotropic growth which is supposed to influence the dopant incorporation. The situation is complicated by the different growth modes, vapor-liquid-solid (VLS) and

* Correspondence: m.lepsa@fz-juelich.de
[2]Peter Grünberg Institute (PGI-10), Forschungszentrum Jülich GmbH, 52425 Jülich, Germany
[3]JARA-Fundamentals of Future Information Technology (JARA-FIT), Jülich-Aachen Research Alliance, Jülich, Germany
Full list of author information is available at the end of the article

VS, of the participating facets [29, 30] and peculiar crystal phase polytypism [31]. All these specific characteristics result in inhomogeneous dopant distribution, both axially and radially [29, 32, 33]. The group IV element Si has been commonly used as n-type dopant for MBE grown III-V thin films. However, Si is known to exhibit amphoteric behavior, i.e., Si atoms can be incorporated as donors on cation lattice sites or acceptors on anion lattice sites, depending on the substrate orientation and growth conditions [34, 35]. This behavior was observed also in nanowires being correlated with the different crystal orientations of the facets involved in the growth, growth mechanisms, and growth temperature [29, 36, 37]. On the other hand, the group VI element Te is a very effective n-type dopant in epilayers [38] presenting no risk of amphoteric behavior. Additionally, Te has some other advantages: a lower ionization energy compared to other n-type dopants commonly used in III-V material systems which potentially leads to the achievement of higher doping levels [39]; a lower diffusion coefficient [40] and weaker memory effect in comparison to other group VI elements, namely, S and Se, which are important for abrupt interfaces [41]. The exclusively n-type dopant behavior of Te has been reported for Au-catalyzed [42] and self-catalyzed GaAs nanowires showing the potential to rich high-doping concentration but also the impact on the wire morphology and crystal structure [43, 44].

In this communication, we investigate Te-doping in InAs NWs, providing information about the impact of doping on the NW morphology and the switching between the ZB and the WZ structure within the VS growth in the presence of Te. Investigations based on scanning electron microscopy (SEM) disclosed a strong impact of Te on the NW morphology. High-resolution transmission electron microscopy (HR-TEM) [45] and X-ray diffraction (XRD) measurements served to evidence a change in the ZB/(WZ + ZB) ratio and electrical two-point measurements showed an increase in conductivity with raising Te-doping level.

## Methods/Experimental

InAs NWs were grown in the VS mode without the use of any foreign catalyst on n-type Si (111) substrates.

### Substrate Preparation

Prior to growth, the substrates were cleaned using HF and DI-water. A consecutive hydrogen peroxide treatment for 45 s leads to the formation of a few angstrom thick SiO2 film containing pinholes, which serve as nucleation centers for the NW growth [20]. After the oxidation, the substrates were immediately transferred into the load-lock in which they were heated to 200 °C for 45 min. This was followed by a degassing step within the preparation chamber, heating the samples at 400 °C for another 45 min.

### Growth of the InAs Nanowires

The NWs were grown at a substrate temperature of 475 °C for 1:20 h in an Omicron Pro 100 molecular beam epitaxy (MBE) chamber. An in-growth rate of 0.1 $\mu mh^{-1}$ was used for the NW growth. Arsenic was provided via an As cracker-cell and the As4-beam equivalent pressure (BEP) was adjusted to values of $2.3 \times 10^{-5}$ Torr and $3.3 \times 10^{-5}$ Torr. The first sample series (series A) was grown at higher As-partial pressure compared to a second growth series (series B) (cf. Table 1), while keeping all other parameters constant. Tellurium was supplied during the growth using stoichiometric GaTe. The operation temperature of the effusion cell was varied between 401 °C and 562 °C based on calibrations conducted on Te-doped GaAs layers via Hall-measurements. The GaTe-cell temperatures 401 °C, 447 °C, 500 °C, and 561 °C correspond to a carrier concentration of about $1 \times 10^{15} cm^{-3}$, $4 \times 10^{16} cm^{-3}$, $5 \times 10^{17} cm^{-3}$, and $6 \times 10^{19} cm^{-3}$ respectively, in GaAs (100) layers used for calibration.

### Device Processing

In order to process two-point contacts, the NWs were mechanically transferred on a pre-patterned Si substrate which was covered with 200 nm SiO2. A schematic diagram of the contacting steps is provided in Additional file 1: Figure S1. Prior to metal deposition, the wires were spin-coated by a three-layer system of 50 K (AR-P639.04), 50 K, and 950 K (AR-P679.04) PMMA resist upon which the contact shape was defined via e-beam lithography. After development, the contact area was passivated by diluted 3.5% ammonium polysulfide ($H_2O$: $(NH4)_2S_3$, 34:1) at 60 °C for 30 min. The electrodes, consisting of 100 nm titanium and 40 nm gold, were deposited via an electron beam evaporator.

The complete list of samples investigated via SEM, TEM, XRD, and electrical measurements is presented in Table 1. Here, the letters A, B, and C indicate the sample series which were grown each at different As-partial pressures

**Table 1** As4-BEP and GaTe-cell doping temperature of the samples used for analysis

| Sample | As4-BEP [$10^{-5}$ Torr] | GaTe temp. [°C] |
| --- | --- | --- |
| A1 | 3.3 | 0 |
| B1 | 2.3 | 0 |
| A2 | 3.3 | 401 |
| B2 | 2.3 | 401 |
| A3 | 3.3 | 447 |
| B3 | 2.3 | 447 |
| B4 | 2.3 | 462 |
| A4 | 3.3 | 500 |
| C1 | 3.0 | 500 |
| A5 | 3.3 | 561 |

but apart from that under equal conditions. A GaTe temperature of 0 °C corresponds to a closed cell shutter.

## Results and Discussion
### Morphology
SEM imaging was used in order to investigate the influence of Te-doping on the wire morphology. The results are presented in Fig. 1. Every data point on the graphs represents the mean of at least 40 wires and the error bar their standard deviation.

Figure 1a shows the morphology of wire series A grown at an As-partial-pressure of about $3.3 \times 10^{-5}$ Torr. The GaTe-cell temperature ranged from 0 °C to 561 °C. Taking the error bar into account, no distinct trend of the NW diameter and length is observed until a cell temperature of 500 °C. However, at 561 °C the supply of Te is clearly

detrimental, leading to a strong increase in diameter and decrease in NW length. Growth series B, depicted in Fig. 1b, has been grown at a comparably lower As pressure of $2.3 \times 10^{-5}$ Torr. The inset shows an exemplary SEM side view of a grown sample, exhibiting InAs NWs and clusters on the substrate surface. Further SEM images of series A and B are shown in Additional file 1: Figure S2. Here, a GaTe-cell temperature range from 0 °C to 462 °C was explored. We observe a decrease in length when Te is added during growth for series B at a cell temperature of 401 °C. Comparing the measurements of series A and B in the same temperature interval, it is observed that in particular the decrease of NW length is more distinct at comparably lower As pressures (series B). However, the same overall trend, i.e., a decrease in NW length is observed for both series and an increase in diameter is observed for series A.
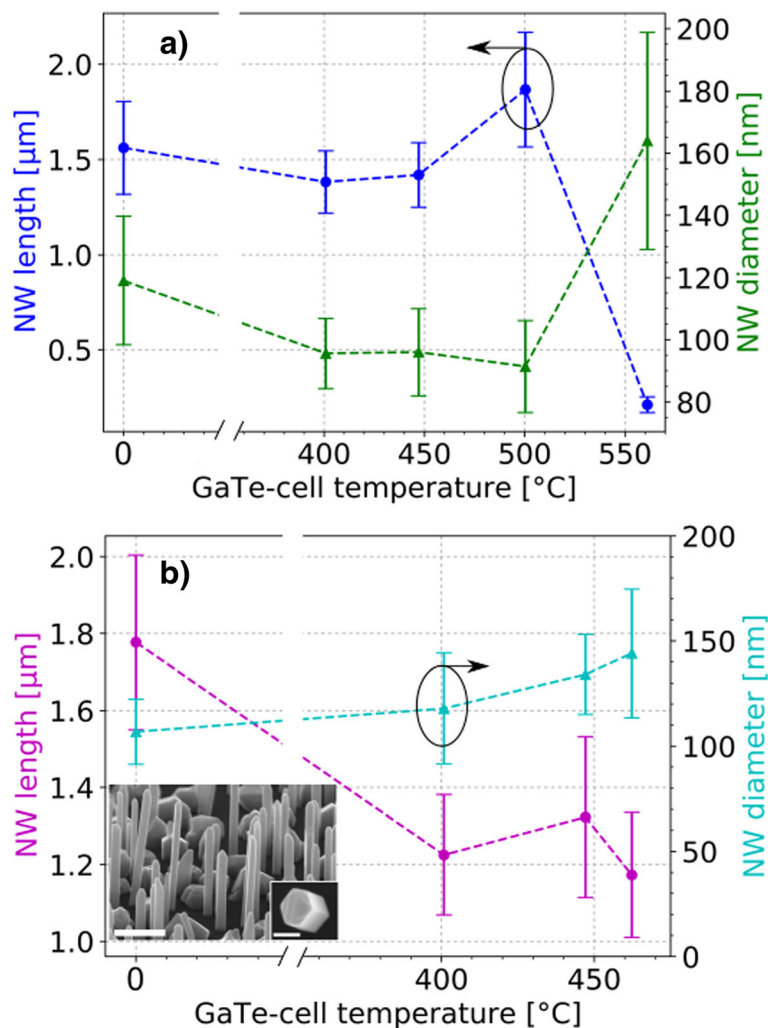


**Fig. 1** Nanowire morphology. Nanowire mean length and diameter at different GaTe-cell temperatures. **a** Series A was grown at an As-partial-pressure of about $3.3 \times 10^{-5}$ Torr. **b** Series B was grown at an As-partial pressure of $2.3 \times 10^{-5}$ Torr. The broken lines are guidance for the eyes. The SEM micrograph shown in the inset depicts undoped InAs NWs surrounded by crystallites formed during growth. The scale bar is 300 nm and 120 nm, respectively

Si doping leads similarly to an increased diameter and decreased length for InAs and GaAs, independently of the growth method (MBE or metalorganic vapor phase epitaxy (MOVPE)) [46, 47]. The same change in dimensions was observed for Te-doping of catalyst-free GaAs NWs grown by MBE [44]. It seems that independent of the used material system, i.e., IIIV materials doped with group IV (InAs/Si, GaAs/Si) or group VI materials (GaAs/Te, InAs/Te), the same overall trend regarding morphology is observed.

Te exhibits a rather large covalent radius with respect to the host lattice atoms and can therefore act as surfactant [48, 49]. The observed behavior might thus be originated in a decreased diffusivity of the In atoms caused by Te. This in turn could cause the increase in radial growth and a decrease in length as the In adatoms are hindered on their way to the NW tip where they control the growth [46]. Comparing Fig. 1a (series A) and Fig. 1b (series B), we find that the As pressure influences how the wire morphology is affected by the Te addition. The finding suggests that it might be possible to counteract the diminishing impact of Te on the radial and axial dimension of the InAs wire by increasing the As pressure to a certain extent.
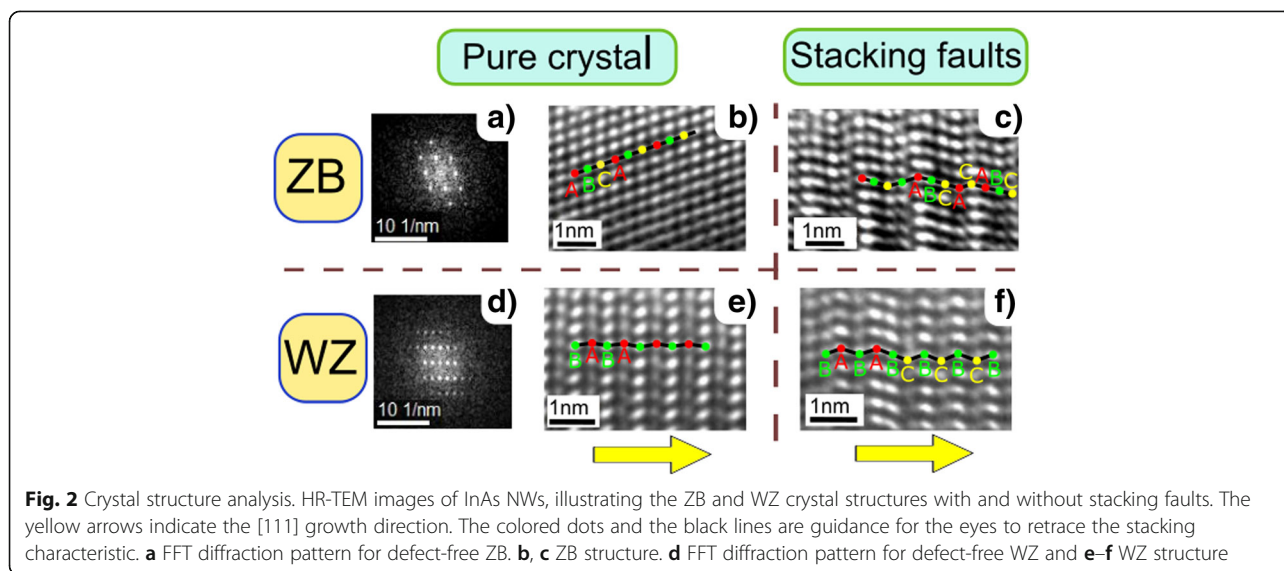
### Crystal Structure

The impact of the Te-dopants on the crystal structure was investigated using TEM and XRD. Adopting the classification used by Caroff et al. [49], a crystal stacking sequence was assigned to a ZB (cf. Fig. 2a) or a WZ (cf. Fig. 2d) segment if the stacking sequence followed exactly four bilayers of atoms. This means …ABCA… was counted as a ZB segment and …ABAB… as a WZ segment. This is illustrated in Fig. 2b, e. Here, every letter represents a bilayer of atoms. Some wire sections are interrupted by

stacking faults (SFs) consisting of a missing or excess layer within the crystal sequence, as presented in Fig. 2c, f. Albeit rarely observed, rotational twinning is present in some segments as well (not shown here).

Crystal sections were identified as ZB or WZ segments only if one full sequence consisting of four bilayers of atoms was observed. The remaining sections were attributed to SFs or rotational twins.

The crystal structure at three different doping levels evaluated according to the explained characteristics is illustrated in Fig. 3. Different WZ and ZB areas are highlighted. However, for the analysis, only individual segments were counted. In order to quantify the influence of the Te-doping onto the NW crystal structure, a total length of about 150 nm of segments from 10 NWs for each doping level was analyzed and averaged (cf. Fig. 3b–d). The ZB/(WZ + ZB) segment ratio was determined by counting the number of single ZB and WZ segments. The samples B1, B3, C1, and A4 at 0 °C, 447 °C, and 500 °C were analyzed (cf. Fig. 4), respectively. We observe an enhancement of the ZB/(WZ + ZB) segment ratio with increasing GaTe-cell temperature. This trend is illustrated in Fig. 4. Comparing the first two data points (0 °C and 447 °C), the enhanced ratio is due to a stronger increase in ZB segments in comparison to the increase of WZ segments from the undoped to the lowest doping temperature (cf. inset Fig. 4). Both structure types are enhanced, and the number of SFs is decreased. However, the trend differs for the third point. When comparing the highest with the lowest doping level (500 °C and 447 °C), we find that the number of WZ segments decreases and the number of ZB segments stays almost constant (cf. inset Fig. 4) while the number of SFs increases. This leads to a raised ratio. Still, the ZB section is promoted in comparison to the undoped case. Finally, the
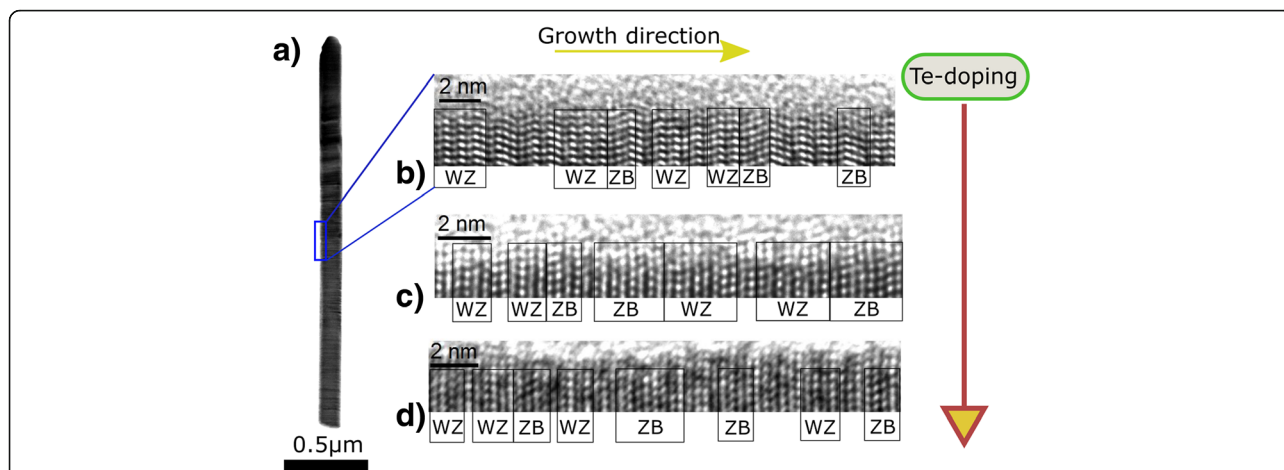


**Fig. 2** Crystal structure analysis. HR-TEM images of InAs NWs, illustrating the ZB and WZ crystal structures with and without stacking faults. The yellow arrows indicate the [111] growth direction. The colored dots and the black lines are guidance for the eyes to retrace the stacking characteristic. **a** FFT diffraction pattern for defect-free ZB. **b**, **c** ZB structure. **d** FFT diffraction pattern for defect-free WZ and **e**–**f** WZ structure

**Fig. 3** Te-doping influence on the crystal structure. TEM images depicting the crystal structure in undoped and Te-doped InAs NWs. **a** Side view of an InAs NW. **b**–**d** HR-TEM images of the InAs NW crystal structure (image turned 90° clockwise). The WZ and ZB areas are labeled. The following samples and GaTe-cell temperatures were chosen: **b** B1 (As$_4$-BEP = 2.3 × 10$^{-5}$ Torr), undoped, i.e., 0 °C. **c** B3 (As$_4$-BEP = 2.3 × 10$^{-5}$ Torr), 447 °C. **d** C1 (As$_4$-BEP = 3.0 × 10$^{-5}$ Torr), 500 °C

findings show that the Te-doping indeed enhances the ZB/(WZ + ZB) segment ratio. However, it remains ambiguous if the formation of ZB segments is strictly promoted by Te incorporation.

In order to complement the observations made by TEM, XRD measurements were performed. We conducted φ-scans focusing on the cubic (220) and the hexagonal [10–15] reflexes. These reflexes can be unambiguously attributed to the ZB and the WZ structure, respectively. The measurement of the respective intensities allowed to extract the $I_{ZB}/(I_{ZB} + I_{WZ})$ intensity ratio. The φ-scans depicted in Fig. 5a, served to determine the relative intensities of the ZB and the WZ peaks at each GaTe-cell doping temperature. For the ZB reflex, six
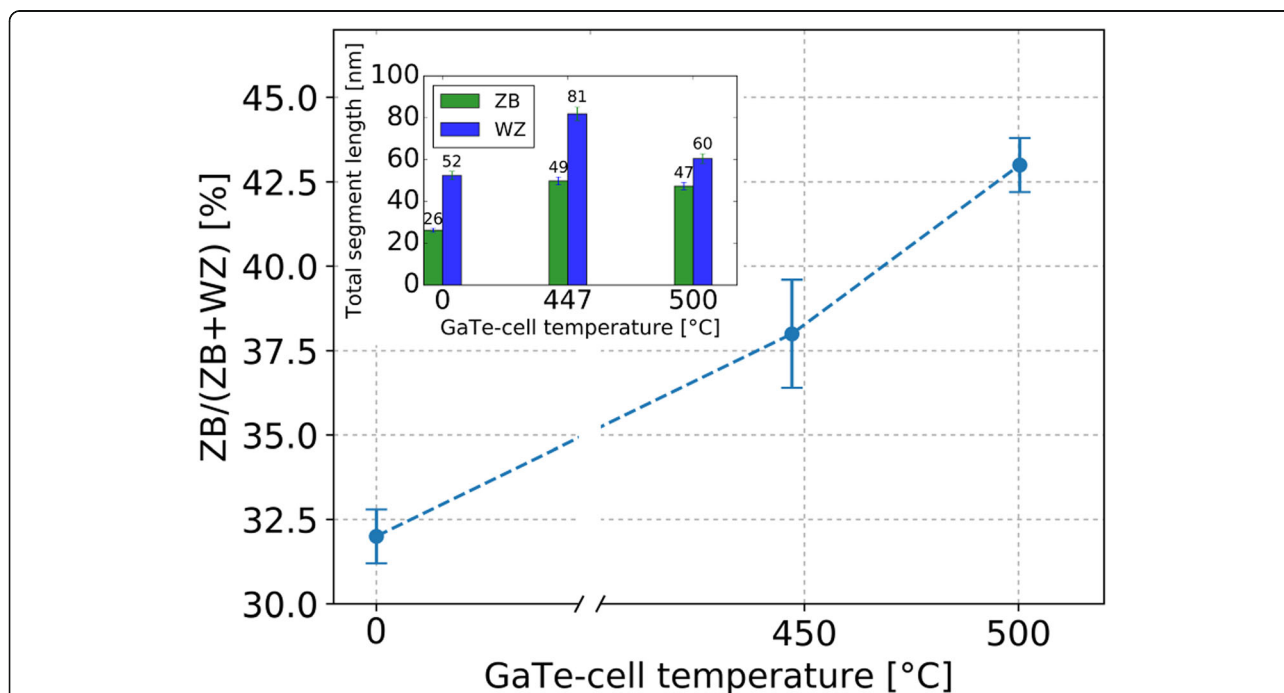


**Fig. 4** Ratio between ZB and WZ segments. Ratio of the number of ZB segments and the total number of segments identified as WZ or ZB in dependence on the GaTe-cell temperature. For the first two measurements B1 and B3 have been analyzed. At 500 °C, the results of wires C1 and A4 were merged as they were grown at similar As-BEP. The bar plot in the inset depicts the accumulated length of all WZ and ZB segments present in the NW at the indicated cell temperature, respectively
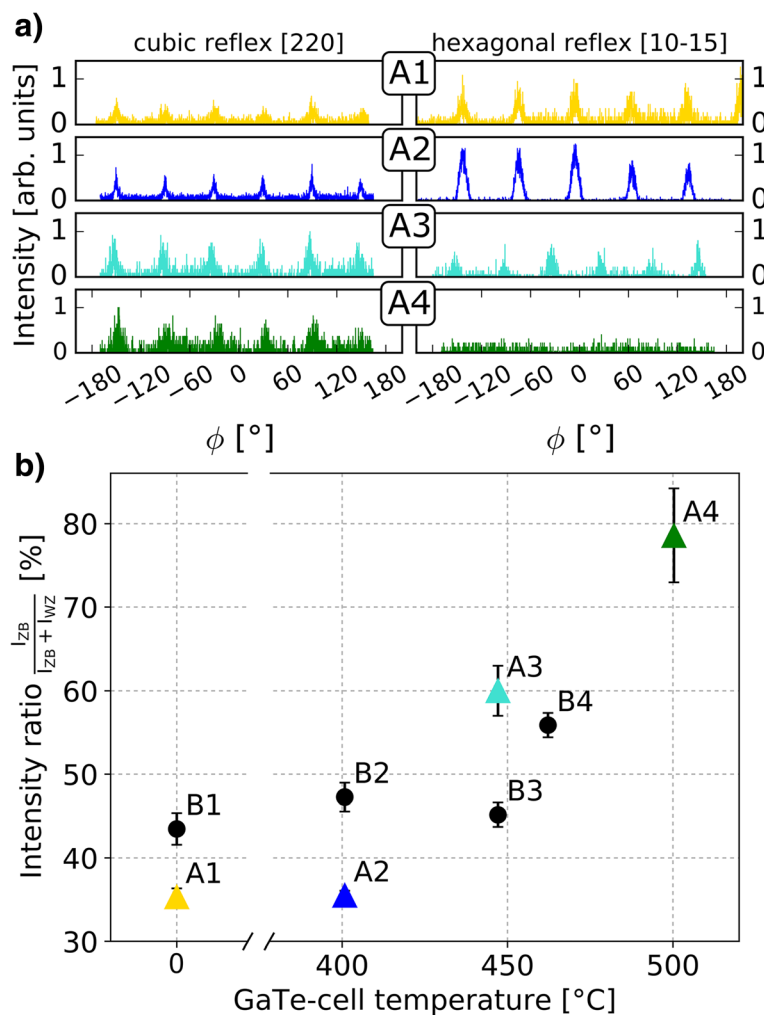
Güsken *et al. Nanoscale Research Letters* (2019) 14:179

Page 6 of 10



**Fig. 5** X-ray analysis of the lattice structure. **a** φ scans obtained via X-ray measurements on InAs NWs A1-A4. **b** Resulting $I_{ZB}/(I_{WZ} + I_{ZB})$ intensity ratio vs. GaTe-cell temperature. The triangular data points are extracted from the measurements depicted in (**a**) for samples A1–A4. The black dots indicate the data points of samples B1–B4

peaks occur even though the cubic lattice should only lead to a 3-fold symmetry. We assign these peaks to symmetric twins in the ZB structure. The six-fold symmetric peaks occurring in the WZ scan are characteristic for the hexagonal crystal structure and match our expectations. Here, the signal intensity of InAs surface crystallites (cf. inset in Fig. 1) is assumed to be two orders of magnitude smaller than the NW signal [50] and can be thus neglected. The corresponding intensity ratio $I_{ZB}/(I_{ZB} + I_{WZ})$ is plotted in Fig. 5b (colored triangles for series A). It shows an increase of the $I_{ZB}/(I_{ZB} + I_{WZ})$ intensity ratio with increasing GaTe-cell temperature, becoming apparent after 401 °C for series A. This result is in accordance with the observation already obtained from the TEM analysis. Note that the given intensity ratios do not represent the real ZB/WZ proportion but constitute a qualitative result. This is due to the fact that different reflexes are of different intensity, according to the structure factor which has not been taken into account explicitly. However, the comparison among the data points remains valid. The same reflex-sensitive measurement was conducted for series B which was grown at a lower As pressure than series A presented above. The results depicted in Fig. 5b (black dots) show a similar trend as the A series, i.e., an increase in the ZB/(WZ + ZB) intensity ratio at higher cell temperatures. However, the impact of the Te atoms on the crystal structure is less distinct in comparison to higher As pressures and a clear increase is only observed at 462 °C. Although series B shows only an enhancement of the ZB/(WZ + ZB) intensity ratio in the XRD for the highest GeTe-cell temperature of 462 °C, series A clearly exhibits an increase at 447 °C and 500 °C cell temperature. This observation suggests that the As atoms facilitate the

incorporation of Te atoms, which in turn leads to a change in crystal structure. Hence, a stronger impact on the ZB/(WZ + ZB) ratio is observed for the respective higher As pressure. The decrease of the intensity ratio at 447 °C in Fig. 5b might be due to shadowing effects as the NW density for sample B3 was above average, though this is not yet fully understood.

From the TEM results presented above, one concludes that the NWs which were grown under Te supply show an increased number of ZB and WZ segments and hence less SFs compared to the undoped case. Further, the XRD measurements indicate that the ZB/(WZ + ZB) intensity ratio increases with increasing Te-doping level (at higher temperatures) which is qualitatively in line with the TEM measurements. In contrast to common elements used for doping of III-V materials such as Si (InAs/Si [30], GaAs/Si), C (GaAs/C), or Be (GaAs/Be), Te clearly affects the crystal structure of the NW. The promotion of the observed ZB formation might originate from a change of surface energies, lowering the energy barrier for ZB nucleation. This was equally observed in zinc doped InP nanowires [51] where Au-catalyzed VLS growth was used. However, further research is needed to clarify the underlying mechanism.

## Electrical Measurements

The conductivity defined by $\sigma = A \cdot R \cdot L^{-1}$ w was extracted from two-point measurements using Ti/Au contacts. Here, A is the hexagonal cross-section of the wire with $A = 3\sqrt{3}d^2_{\mathrm{NW}}/8$ where $d_{\mathrm{NW}}$ is the maximal diameter, R the resistance, and Lw the distance between the electric contacts. $L_w$ and $d_{\mathrm{NW}}$ have been measured individually for every wire via SEM imaging. Exemplary I–V characteristics of undoped and doped InAs NWs are presented in Fig. 6a–d. The graphs show the expected ohmic behavior due to the surface accumulation layer of InAs [6, 52]. The conductivity in dependence on the doping level was determined based on the I–V measurements and the NW geometry. The resulting dependence between the conductivity and the GaTe-cell temperature is illustrated in Fig. 6e. At each temperature at least 20 NWs were examined for series A. Comparing undoped and doped wires, an increase in average conductivity of about one order of magnitude at the highest doping level is observed. At a GaTe-cell temperature of 500 °C an average conductivity of about 80 S/cm was determined (compared to about 8 S/cm for 0 °C). Although the spread in conductivity for higher doping levels is quite distinct, our observation shows that incorporation of Te indeed has a strong impact, leading to an increased conductivity in average. The comparison of the XRD and the conductivity measurement suggests that below 401 °C the impact of Te on the crystal structure and transport properties plays merely a minor role. The large variance in conductivity of InAs NWs mentioned above has

been similarly reported in the literature [53]. No trend of the conductivity was observed with respect to a change in NW diameter or contact spacing, as expected [26]. Thus, we exclude the differing aspect ratio as a source of error. We identify three main reasons responsible for the strong variance in conductivity: (i) the contact passivation method using ammonium polysulfide could lead to a heterogeneous contact quality. (ii) The wire surface is not passivated and surface states can be influenced by an inhomogeneous saturation of the dangling bonds at the wire side facets via water and oxygen which finally results in non-uniform surface oxidation. This in turn has a strong impact on the transport characteristics, leading to large errors [54]. One way to prevent these heterogenous surface states is the passivation via in situ deposition of $Al_2O_3$ [53, 55]. (iii) Inhomogeneous doping along the NW, as observed for Si doping [26], might also cause the large data spread, although we tried to exclude that by placing the contacts centered for each wire. Finally, variations in NW length (cf. Fig. 1) and density can lead to shadowing effects, preventing from homogeneous Te incorporation across the sample. However, more systematic investigations are needed to identify the origin of the large variance observed. Additionally, conductivity measurements for NWs of series B grown at a comparably lower As pressure were conducted. Here, at least six wires were measured for each GaTe-cell temperature. The results depicted in Fig. 6e show a similar behavior as the ones discussed above for series A. The conductivity of InAs NWs is increased for higher GaTe-cell temperatures. However, the effect is less distinct in comparison with series A, grown at a higher As pressure. Comparing the conductivities of both series at 401 °C and 447 °C in Fig. 6e, we find that the values for series A are about twice as large as the ones found for B. The XRD results presented above (cf. Fig. 5) illustrate that the crystal structure in series A is more strongly affected by the Te incorporation than in series B. The combination of both findings indicates that the raised conductivity is related to the change in crystal structure, i.e., the increased ZB/(WZ + ZB) intensity ratio. It is known from the literature that a modification in the InAs NW crystal structure from WZ dominated toward ZB dominated, enhances conductivity [50, 53, 56]. Based on TEM investigations on $InAs_{1-x}Sb_x$ NWs, Sourribes et al. reported an increase in conductivity by 1.5 for a gain in NW ZB fraction from 20 to 80% [50]. Our TEM results (cf. Fig. 4) show a raised ZB/(WZ + ZB) ratio from 32% (undoped NW) to 43% (maximum doped NW) while the averaged conductivity value increases by about a factor of 10. This comparison suggests that the altered crystal structure is not the only reason for the conductivity enhancement. Although the modification of the crystal structure affects the carrier transport, the effect observed is probably likewise due to an augmented carrier density induced by Te acting as a donor.
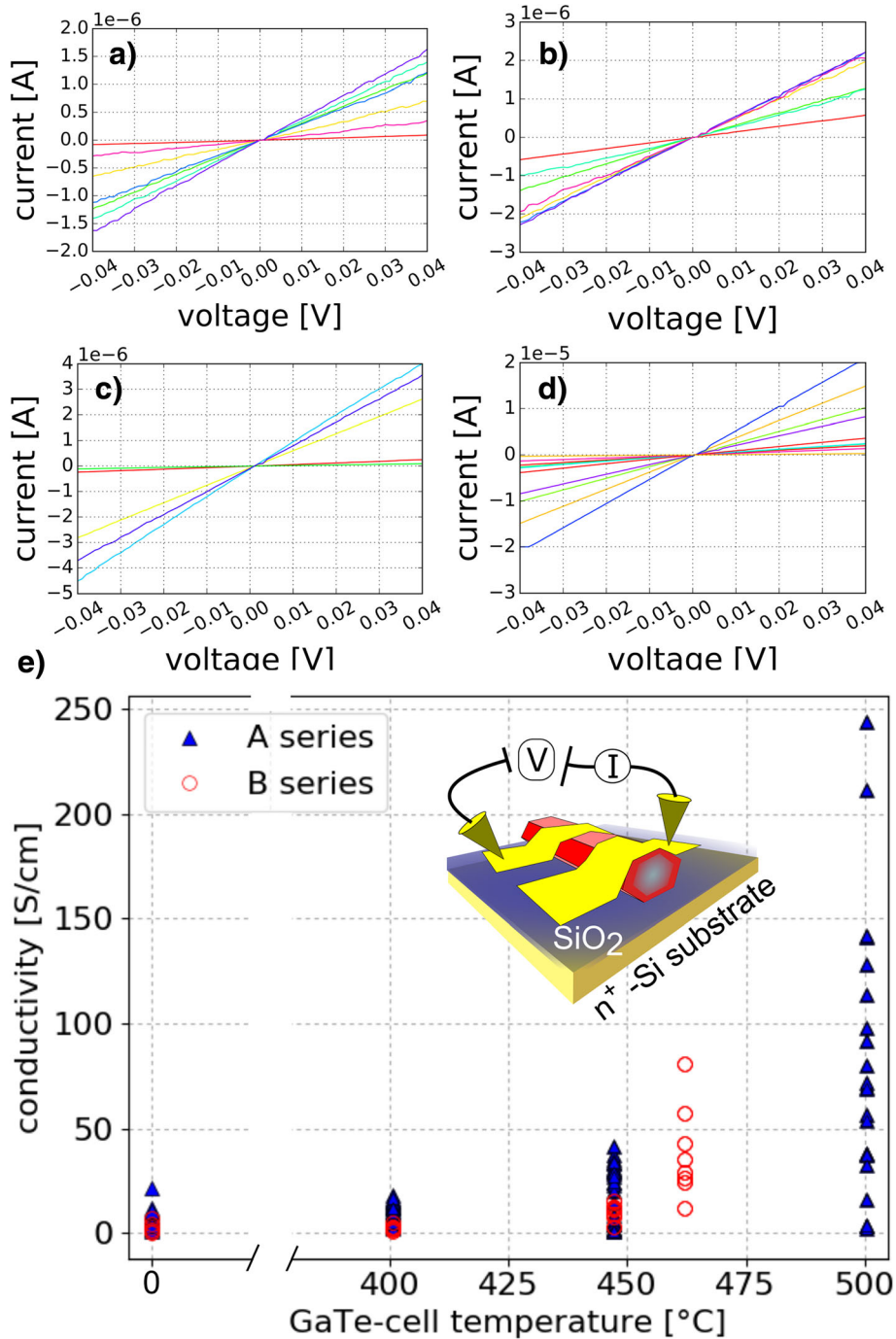
**Fig. 6** Electrical characterization. **a**–**d** Exemplary I–V measurements of InAs NWs at a GaTe-cell temperature of 0 ℃, 401 ℃, 447 ℃, and 500 ℃ (series A) measured via two-point contacts. **e** Determined conductivity values of Te-doped InAs NWs in dependence of GaTe-cell temperature for the A (high As-BEP) and B (low As-BEP) series. The inset shows a schematic of the electrical measurement configuration

## Conclusion

In summary, we have grown Te-doped catalyst-free InAs NWs on Si (111) substrates via the vapor-solid growth method. Te was provided by a GaTe-cell enabling the growth of Te-doped InAs NWs at different doping levels by adjusting the cell temperature. Two sample series grown at different As-BEPs were characterized by SEM, TEM, XRD, and electrical measurements. We have shown that Te changes the NW morphology leading to an overall trend of an increased radial and decreased axial growth rate. The impact is stronger at comparably lower As-partial pressures. TEM and XRD measurements disclosed that the

NW crystal structure is affected by Te addition, resulting in an increase of the ZB/(WZ + ZB) ratio for both growth series. The influence on the NW crystal structure grown at comparably higher As-BEP was more enhanced than observed for NWs grown at lower As-BEP. Electrical two-point measurements demonstrated an increase in average conductivity for wires grown under Te supply. This was observed for two growth series, grown at different As pressures. The comparison between the two sample series showed that the crystal and electrical properties of InAs NWs are more strongly affected by Te addition at higher As pressures. The result indicates that the improved average conductivity is strongly related to the change in the crystal structure, i.e., the increase in ZB/(WZ + ZB) ratio. We attribute the enhanced transport properties to both the incorporated group VI element Te acting as a donor as well as an altered crystal structure. This work constitutes an important contribution in order to extend the options for NW doping which is of great interest to counteract the degradation of transport properties by SFs.

## Additional file

**Additional file 1: Figure S1.** Schematic illustration of the NW device processing: (a) resist coating, (b) e-beam writing, (c) development, (d) metallization, (e) lift-off process, and (f) the resulting contacted nanowire. The inset in f) shows a SEM topview of a metal contacted InAs NW. **Figure S2.** SEM side images of the doped and undoped InAs nanowires. a) growth series A and b) growth series B. The GaTe-cell temperature is indicated for each image at the top left. (DOCX 1610 kb)

## Abbreviations
As: Arsenic; BEP: Beam equivalent pressure; C: Carbon; GaAs: Gallium arsenide; GaTe: Gallium telluride; HR-TEM: High-resolution transmission electron microscopy; InAs: Indium arsenide; MBE: Molecular beam epitaxy; MOVPE: Metalorganic vapor phase epitaxy; NW: Nanowire; SEM: Scanning electron microscopy; SF: Stacking fault; Si: Silicon; Te: Tellurium; VS: Vapor-solid; WZ: Wurtzite; XRD: X-ray diffraction; ZB: Zinc-blende

## Availability of Data and Materials
They are all in the main text and figures.

## Authors' Contributions
NAG conducted the MBE growth, the NW contacting, the SEM imaging, the electrical measurements, and the analysis, and wrote the manuscript. TR supervised the MBE growth, conducted the TEM, and contributed to the manuscript. GM conducted the X-ray measurements and supported the X-ray analysis. MIL and DG modified the manuscript writing and guided the research. All the authors discussed the results. All authors read and approved the final manuscript.

## Competing Interests
The authors declare that they have no competing interests.

## Publisher's Note
Springer Nature remains neutral with regard to jurisdictional claims in published maps and institutional affiliations.

## Author details
[1]Peter Grünberg Institute (PGI-9), Forschungszentrum Jülich GmbH, 52425 Jülich, Germany. [2]Peter Grünberg Institute (PGI-10), Forschungszentrum Jülich GmbH, 52425 Jülich, Germany. [3]JARA-Fundamentals of Future Information Technology (JARA-FIT), Jülich-Aachen Research Alliance, Jülich, Germany.

## References
1. Khanal DR, Wu J (2007) Gate coupling and charge distribution in nanowire field effect transistors. Nano Lett 7(9):2778–2783. https://doi.org/10.1021/nl071330l
2. Breuer S, Pfüller C, Flissikowski T, Brandt O, Grahn HT, Geelhaar L, Riechert H (2011) Suitability of au- and self-assisted GaAs nanowires for optoelectronic applications. Nano Lett 11(3):1276–1279. https://doi.org/10.1021/nl104316t
3. Xiang J, Lu W, Hu Y, Wu Y, Yan H, Lieber CM (2006) Ge/Si nanowire heterostructures as high-performance field-effect transistors. Nature 441(7092):489–493. https://doi.org/10.1038/nature04796
4. Noor Mohammad S (2011) Why self-catalyzed nanowires are most suitable for large-scale hierarchical integrated designs of nanowire nanoelectronics. J Appl Phys 110(8):084310. https://doi.org/10.1063/1.3624585
5. Das A, Ronen Y, Most Y, Oreg Y, Heiblum M, Shtrikman H (2012) Zero-bias peaks and splitting in an Al-InAs nanowire topological superconductor as a signature of Majorana fermions. Nat Phys 8(12):887–895. https://doi.org/10.1038/nphys2479.1205.7073
6. Piper LFJ, Veal TD, Lowe MJ, McConville CF (2006) Electron depletion at InAs free surfaces: doping-induced acceptor like gap states. Phys Rev B 73(19):195321. https://doi.org/10.1103/PhysRevB.73.195321
7. Dayeh SA, Aplin DPR, Zhou X, Yu PKL, Yu ET, Wang D (2007) High electron mobility InAs nanowire field-effect transistors. Small 3(2):326–332. https://doi.org/10.1002/smll.200600379
8. Dayeh SA (2010) Electron transport in indium arsenide nanowires. Semicond Sci Technol 25(2):24004. https://doi.org/10.1088/0268-1242/25/2/024004
9. Björk MT, Fuhrer A, Hansen AE, Larsson MW, Fröberg LE, Samuelson L (2005) Tunable effective g factor in InAs nanowire quantum dots. Phys Rev B 72(20):201307. https://doi.org/10.1103/PhysRevB.72.201307
10. Liang D, Gao XPA (2012) Strong tuning of Rashba spin–orbit interaction in single InAs nanowires. Nano Lett 12(6):3263–3267. https://doi.org/10.1021/nl301325h
11. Estevez Hernandez S, Akabori M, Sladek K, Volk C, Alagha S, Hardtdegen H, Pala MG, Demarina N, Gru¨tzmacher D, Schäpers T (2010) Spin-orbit coupling and phase coherence in InAs nanowires. Phys Rev B 82(23):235303. https://doi.org/10.1103/PhysRevB.82.235303
12. Nadj-Perge S, Frolov SM, Bakkers EP, Kouwenhoven LP (2010) Spin-orbit qubit in a semiconductor nanowire. Nature 468(7327):1084–1087. https://doi.org/10.1038/nature09682.1011.0064
13. Leijnse M, Flensberg K (2013) Coupling spin qubits via superconductors. Phys Rev Lett 111(6):060501. https://doi.org/10.1103/PhysRevLett.111.060501.1303.3507
14. Lutchyn RM, Sau JD, Das Sarma S (2010) Majorana fermions and a topological phase transition in semiconductor-superconductor heterostructures. Phys Rev Lett 105(7):077001. https://doi.org/10.1103/PhysRevLett.105.077001.1002.4033
15. Perea DE, Allen JE, May SJ, Wessels BW, Seidman DN, Lauhon LJ (2006) Three-dimensional nanoscale composition mapping of semiconductor nanowires. Nano Lett 6(2):181–185. https://doi.org/10.1021/nl051602p
16. Tambe MJ, Ren S, Gradecak S (2010) Effects of gold diffusion on n-type doping of GaAs nanowires. Nano Lett 10:4584–4589. https://doi.org/10.1021/nl102594e
17. Tomioka K, Fukui T (2014) Recent progress in integration of III–V nanowire transistors on Si substrate by selective-area growth. J Phys D Appl Phys 47: 394001. https://doi.org/10.1088/0022-3727/47/39/394001
18. Memisevic E, Hellenbrand M, Lind E, Persson AR, Sant S, Schenk A, Svensson J, Wallenberg R, Wernersson L-E (2017) Individual defects in InAs/InGaAsSb/GaSb nanowire tunnel field- effect transistors operating below 60 mV/decade. Nano Lett 17:4373–4380. https://doi.org/10.1021/acs.nanolett.7b01455

19. Alexander-Webber JA, Groschner CK, Sagade AA, Tainter G, Gonzalez-Zalba MF, Di Pietro R, Wong-Leung J, Tan HH, Jagadish C, Hofmann S, Joyce HJ (2017) Engineering the Photoresponse of InAs nanowires. ACS Appl Mater Interfaces 9(50):43993–44000. https://doi.org/10.1021/acsami.7b14415

20. Rieger T, Grützmacher D, Lepsa MI (2013) Si substrate preparation for the VS and VLS growth of InAs nanowires. Phys Status Solidi Rapid Res Lett 7(10): 840–844. https://doi.org/10.1002/pssr.201307229

21. Shtrikman H, Popovitz-Biro R, Kretinin AV, Kacman P (2011) GaAs and InAs nanowires for ballistic transport. IEEE J Sel Top Quantum Electron 17:922. https://doi.org/10.1109/JSTQE.2010.2053920

22. Joyce HJ, Wong-Leung J, Gao Q, Tan HH, Jagadish C (2010) Phase perfection in zinc blende and Wurtzite III-V nanowires using basic growth parameters. Nano Lett 10:908–915. https://doi.org/10.1021/nl903688v

23. Tomioka K, Motohisa J, Hara S, Fukui T (2007) Crystallographic structure of InAs nanowires studied by transmission electron microscopy. Jpn J Appl Phys 46:L1102–L1104. https://doi.org/10.1143/JJAP.46.L1102

24. Wei W, Bao XY, Soci C, Ding Y, Wang ZL, Wang D (2009) Direct heteroepitaxy of vertical InAs nanowires on Si substrates for broad band photovoltaics and photodetection. Nano Lett 9(8):2926–2934. https://doi.org/10.1021/nl901270n

25. Dimakis E, Lähnemann J, Jahn U, Breuer S, Hilse M, Geelhaar L, Riechert H (2011) Self-assisted nucleation and vapor–solid growth of InAs nanowires on bare Si (111). Cryst Growth Des 11(9):4001–4008. https://doi.org/10.1021/cg200568m

26. Thelander C, Caroff P, Plissard S, Dey AW, Dick KA (2011) Effects of crystal phase mixing on the electrical properties of InAs nanowires. Nano Lett 11(6):2424–2429. https://doi.org/10.1021/nl2008339

27. Schroer MD, Petta JR (2010) Correlating the nanostructure and electronic properties of InAs nanowires. Nano Lett 10(5):1618–1622. https://doi.org/10.1021/nl904053j.0912.1511

28. Heiss M, Conesa-Boj S, Ren J, Tseng H-H, Gali A, Rudolph A, Uccelli E, Peir F, Morante JR, Schuh D, Reiger E, Kaxiras E, Arbiol J, Fontcuberta i, Morral A (2011) Direct correlation of crystal structure and optical properties in wurtzite/zinc-blende GaAs nanowire heterostructures. Phys Rev B 83(4): 045303. https://doi.org/10.1103/PhysRevB.83.045303.1011.5165

29. Dufouleur J, Colombo C, Garma T, Ketterer B, Uccelli E, Nicotra M, Fontcuberta i Morral A (2010) P-doping mechanisms in catalyst-free gallium arsenide nanowires. Nano Lett 10:1734

30. Casadei A, Krogstrup P, Heiss M, Rohr JA, Colombo C, Ruelle T, Uphadyay S, Sorensen CB, Nygard J, Fontcuberta i, Morral A (2013) Doping incorporation paths in catalyst-free be-doped GaAs nanowires. Appl Phys Lett 102:013117. https://doi.org/10.1063/1.4772020

31. Piccin M, Bais B, Grillo V, Jabeen F, De Franceschi S, Carlino E, Lazzarino M, Romanato F, Businaro L, Rubini S, Martelli F, Franciosi A (2007) Growth by molecular beam epitaxy and electrical characterization of GaAs nanowires. Phys E 37:134

32. Gutsche C, Lysov A, Regolin I, Blekker K, Prost W, Tegude F-J (2011) N-type doping of vapor–liquid–solid grown GaAs nanowires. Nanoscale Res Lett 6: 65. https://doi.org/10.1007/s11671-010-9815-7

33. Dastjerdi MHT, Fiordaliso EM, Leshchenko ED, Akhtari-Zavareh A, Kasama M, Aagesen T, Dubrovskii VG, LaPierre RR (2017) Three-fold symmetric doping mechanism in GaAs nanowires. Nano Lett 17:5875–5882 2017. https://doi.org/10.1021/acs.nanolett.7b00794

34. Schubert EF (1993) Doping in III–V semiconductors Cambridge University Press, Cambridge

35. Sakamoto N, Kirakawa K, Ikoma T (1995) Conduction-type conversion in Si-doped (311) A GaAs grown by molecular beam epitaxy. Appl Phys Lett 67:1444–1446

36. Colombo C, Heiß M, Grätzel M, Fontcuberta i Morral A (2009) Gallium arsenide p-i-n radial structures for photovoltaic applications. Appl Phys Lett 94:173108. https://doi.org/10.1063/1.3125435

37. Dimakis E, Ramsteiner M, Tahraoui A, Riechert H, Geelahaar L (2012) Shell-doping of GaAs nanowires with Si for n-type conductivity. Nano Res 5:796–804. https://doi.org/10.1007/s12274-012-0263-9

38. De-Sheng J, Makita Y, Ploog K, Queisser HJ (1982) Electrical properties and photoluminescence of Te-doped GaAs grown by molecular epitaxy. J Appl Phys 53:999

39. Grundmann M (2006) The physics of semiconductors: an introduction including devices and nanophysics. Springer-Verlag, Berlin

40. Sankaran R (1980) Te doping of vapor phase epitaxial GaAs. J Cryst Growth 50:859

41. Stringfellow GB (1999) Organometallic vapor phase epitaxy: theory and practice, 2nd edn. Academic, New York

42. Salehzadeh O, Chen MX, Kavanagh KL, Watkins SP (2011) Rectifying characteristics of Te-doped GaAs nanowires. Appl Phys Lett 99:182102. https://doi.org/10.1063/1.3658633

43. Orru M, Repiso E, Carapezzi S, Henning A, Roddaro S, Franciosi A, Rosenwaks Y, Cavallini A, Martelli F, Rubini S (2016) A roadmap for controlled and efficient n-type doping of self-assisted GaAs nanowires grown by molecular beam epitaxy. Adv Funct Mater 26:2836–2845. https://doi.org/10.1002/adfm.201504853

44. Suomalainen S, Hakkarainen TV, Salminen T, Koskinen R, Honkanen M, Luna E, Guina M (2015) Te-doping of self-catalyzed GaAs nanowires. Appl Phys Lett 107(1):012101. https://doi.org/10.1063/1.4926494

45. Luysberg M, Heggen M, Tillmann K (2016) FEI Tecnai G2 F20. J Large-Scale Res Facil JLSRF 2:77. https://doi.org/10.17815/jlsrf-2-138

46. Dimakis E, Ramsteiner M, Huang CN, Trampert A, Davydok A, Biermanns A, Pietsch U, Riechert H, Geelhaar L (2013) In situ doping of catalyst-free InAs nanowires with Si: growth, polytypism, and local vibrational modes of Si. Appl Phys Lett 103(14). https://doi.org/10.1063/1.4824344

47. Wirths S, Weis K, Winden A, Sladek K, Volk C, Alagha S, Weirich TE, von der Ahe M, Hardtdegen H, Lüth H, Demarina N, Grützmacher D, Schäpers T (2011) Effect of Si-doping on InAs nanowire transport and morphology. J Appl Phys 110(5):053709. https://doi.org/10.1063/1.3631026

48. Wixom RR, Rieth LW, Stringfellow GB (2004) Te surfactant effects on the morphology of patterned (001) GaAs homoepitaxy. J Cryst Growth 269(2–4): 276–283. https://doi.org/10.1016/j.jcrysgro.2004.05.077

49. Caroff P, Bolinsson J, Johansson J (2011) Crystal phases in III-V nanowires: from random toward engineered polytypism. IEEE J Sel Top Quantum Electron 17(4):829–846. https://doi.org/10.1109/JSTQE.2010.2070790

50. Sourribes MJL, Isakov I, Panfilova M, Liu H, Warburton Pa (2014) Mobility enhancement by Sb-mediated minimisation of stacking fault density in InAs nanowires grown on silicon. Nano Lett 14(3):1643–1650. https://doi.org/10.1021/nl5001554

51. Algra RE, Verheijen MA, Borgström MT, Feiner L-F, Immink G, van Enckevort WJP, Vlieg E, Bakkers EPaM (2008) Twinning superlattices in indium phosphide nanowires. Nature 456(7220):369–372. https://doi.org/10.1038/nature07570.0807.1423

52. Noguchi M, Hirakawa K, Ikoma T (1991) Intrinsic electron accumulation layers on reconstructed clean InAs (100) surfaces. Phys Rev Lett 66(17):2243–2246. https://doi.org/10.1103/PhysRevLett.66.2243

53. Potts H, Friedl M, Amaduzzi F, Tang K, Tütüncüoglu G, Matteini F, Alarcon Llado E, McIntyre PC, Fontcuberta i, Morral A (2015) From twinning to pure zincblende catalyst-free InAs (Sb) nanowires. Nano Lett:5–04367. https://doi.org/10.1021/acs.nanolett.5b04367

54. Dayeh SA, Soci C, Yu PKL, Yu ET, Wang D (2007) Influence of surface states on the extraction of transport parameters from InAs nanowire field effect transistors. Appl Phys Lett 90(16):162112. https://doi.org/10.1063/1.2728762

55. Campabadal F, Rafi JM, Zabala M, Beldarrain O, Faigon A, Castan H, Gomez A, Garcia H, Duenas S (2011) Electrical characteristics of metal-insulator-semiconductor structures with atomic layer deposited Al2O3, HfO2, and nanolaminates on different silicon substrates. J Vac Sci Technol B Microelectron Nanom Struct 29(1):01–07. https://doi.org/10.1116/1.3532544

56. Fu M, Tang Z, Li X, Ning Z, Pan D, Zhao J, Wei X, Chen Q (2016) Crystal phase- and orientation-dependent electrical transport properties of InAs nanowires. Nano Lett 16(4):2478–2484. https://doi.org/10.1021/acs.nanolett.6b00045